Towards Practical Bi-Static Polarimetric Imaging Using Commodity mmWave Radars for Material Sensing

Xinghua Sun
Electrical and Computer Engineering
University of Washington
Seattle, USA
xinghua@uw.edu

Akshay Gadre
Electrical and Computer Engineering
University of Washington
Seattle, USA
gadre@uw.edu

Abstract

Accurately identifying materials in real-world environments is critical for applications in robotics, security screening and autonomous systems. While more expensive approaches for material characterization such as spectroscopy or ellipsometry are ill-suited for large scale deployment, RF-based solutions present a new potential low-cost alternative. Prior RF-based material sensing approaches are either too invasive, suffer from lower resolution or are highly specialized in particular materials, presenting a need for a more general-purpose solution.

This paper presents POLySight, a mmWave radar based material sensing solution that uses the polarization of the signals reflected from target objects. POLySight synthesizes a wide-aperture bi-static mmWave radar system by synchronizing distributed commodity radars to extract polarimetry at large incidence angles. The solution extracts the high-resolution polarimetric image of the object from these synchronized measurements by performing synthetic aperture radar based imaging. Finally, we leverage the ratio of the amplitude in co-polarized and cross-polarized received signals to classify solids, liquids and powders. Our evaluation across 36 different materials demonstrates an accuracy of 95.74%, 96.50% and 100% for classifying 23 solids, 8 liquids and 4 powders and a median error of 1.548% in determining the concentration of a sugar-water solution.

CCS Concepts

• **Computer systems organization → Sensor networks**; • **Computing methodologies → Perception**; • **Human-centered computing → Mobile computing**.

Keywords

Wireless Sensing, mmWave, Material Sensing, Polarimetry

ACM Reference Format:
Xinghua Sun and Akshay Gadre. 2026. Towards Practical Bi-Static Polarimetric Imaging Using Commodity mmWave Radars for Material Sensing. In *ACM/IEEE International Conference on Embedded Artificial Intelligence and Sensing Systems (SenSys '26), May 11–14, 2026, Saint Malo, France.* ACM, New York, NY, USA, 14 pages. https://doi.org/10.1145/3774906.3800470

Code and datasets are available at: https://github.com/xsun2445/polysight.

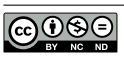

SenSys '26, Saint Malo, France

ACM ISBN 979-8-4007-2309-4/26/05
https://doi.org/10.1145/3774906.3800470

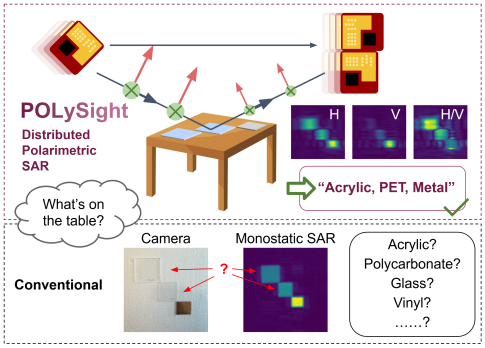

Figure 1: POLySight **develops distributed polarimetric SAR for material detection using commodity mmWave Radars**

1 Introduction

Material sensing in real-world environments plays a critical role in a wide range of applications, including infrastructure inspection, security screening, quality control, and environmental sensing [2, 5, 14, 26, 38]. While data-driven solutions using images can segment and classify common objects, they fail to operate in optically challenging and non-line-of-sight environments. Further, the more traditional visible light material identification solutions rely on optical spectroscopy or ellipsometry that are costly, destructive and only operate at small scale. Thus, recently researchers have turned to radio frequency (RF)-based material sensing solutions as a potential alternative.

Prior material sensing work in the RF domain has explored characterizing materials via multiple approaches. Active material sensing solutions [13, 29] have used acoustic waves to vibrate the object under consideration to recover their mechanical characteristics in the RF response and hence remain **invasive**. Passive pass-through approaches for material sensing using UWB and WiFi estimate the materials by modeling the variation in signal's time-of-flight (ToF) [8] and polarization [43], yet suffer from **low-resolution** due to the large wavelength and require a large radar-cross section of the material being sensed. Passive reflection-based material characterization solutions [26] across the spectrum have primarily focused on leveraging the amplitude and phase response of the material which only works for **significantly separable** reflection behavior. Thus, there is a fundamental gap in practical RF-based solutions that can enable ***high-resolution non-invasive general-purpose*** material sensing.

This paper presents POLySight, a first-of-its-kind reflection-based mmWave imaging and material sensing solution that leverages polarization of the received signal on commodity radars to identify materials. POLySight achieves this by observing that the

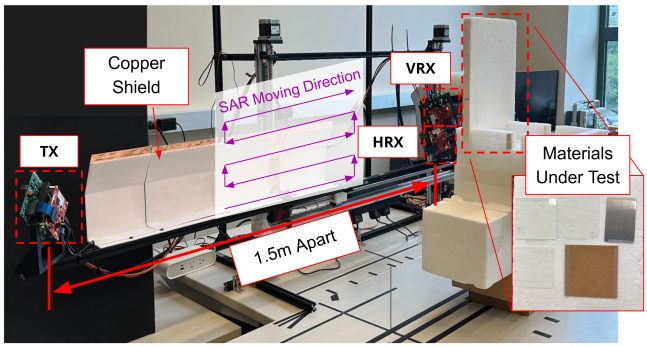

Figure 2: POLySight **develops a multi-static imaging platform by synchronizing spatially separated mmWave radars and mounted them on a 2D motion stage for synthesizing a large aperture to image and classify objects' materials.**

reflected signal from materials only expresses polarization separability at a high incident angle and develops a distributed bi-static polarimetric imaging SAR using commodity off-the-shelf mmWave radars to extract it. We evaluate POLySight on a motion-stage testbed and demonstrate an overall 96.33% classification accuracy across 23 solid materials, 8 liquids and 4 powders.

At the heart of POLySight's approach lies the observation that the polarimetric behavior of materials only expresses itself in reflections at a large incident angle (i.e. Fresnel reflection). Extracting this behavior requires a large distance between the transmit and the receive antennas of an imaging radar that is infeasible for a single commodity radar. Thus, we develop a distributed bi-static mmWave radar configuration that uses the direct path between the radars to synchronize and image the surface of the material using synthetic aperture radar. The rest of this paper presents the above observations and system design in more detail.

1. How do materials express their behavior in reflected signal's polarization at mmWave frequencies? (Sec. 3) We conduct a measurement study using mmWave radars to determine the polarization of the reflected signal from common materials. Our observations demonstrate that the reflected polarization ratio is exactly the same for multiple solid materials which does not help for material sensing. Further, simply using amplitude and phase are not enough to differentiate between many such materials. Finally, we demonstrate that the polarization ratio starts diverging as the incident angle increases and gets closer to the Brewster's angle which increases the contrast between similar materials. We back these measurements with EM simulations to validate the findings. These observations show that common materials are smooth at 77 GHz and interactions with materials mostly follow the Fresnel reflection. To the best of our knowledge, this is the first measurement study and demonstration of polarimetry-based material classification at the mmWave frequencies.

2. Designing a distributed mmWave platform to extract polarization at high incident angles. (Sec. 5) Given the need for a large incident angle to extract separable polarization from the materials, the transmit and receive antennas of the radar need to be separated by a large distance (a meter). Yet, there are no commodity mmWave platforms today that can support such operation. Hence, POLySight seeks to develop a distributed mmWave platform by synchronizing multiple small radars into a synchronized large radar. POLySight designs this platform by engineering a direct path between the radars over-the-air to calibrate and synchronize at both coarse and fine-grained levels. POLySight achieves a synchronization calibration error of 138 Hz between the radars.

3. High-Resolution Imaging and Material Sensing (Sec. 6) We use a 2D linear motion stage for high resolution imaging via SAR to image the target at a resolution of 4.9 mm × 2.8 mm. At the receivers, we align the two images across the axes and capture the polarization ratios between the radars. We then use image segmentation techniques to separate the objects and characterize their materials by observing the polarimetric ratio distribution across their surface.

We implement and evaluate POLySight using 3 commodity TI AWR2243 mmWave radars and a 2D motion stage for SAR imaging and material characterization of 36 materials spanning 23 solids, 8 liquids as well as 4 powders. Our evaluation demonstrates:

- 95.74% accuracy in classifying 23 solid materials, improving to 99.34% with multiple incident angle measurements. (48.46% w/o POLySight)
- 96.5% accuracy in classifying 8 liquids (72.87% w/o POLySight)
- 1.548% concentration detection accuracy for sugar solution.

Contributions: This paper's contributions are as follows:

- We propose a novel material identification framework at mmWave frequencies based on polarization-dependent reflectivity, and validate its effectiveness through proof-of-concept experiments.
- We design and implement the multi-static SAR system capable of capturing linear polarization channels at arbitrary angles using spatially separated and distributed commodity mmWave radars.
- We developed a phase-level synchronization technique for distributed radars, achieving sub-wavelength precision for SAR imaging.

Limitations: Given the nascent nature of our work, our simplified single interface specular reflection model has several limitations. **(1)** First, the current system assumes a relatively flat surface on the material to ensure the specular reflection. While SAR improves imaging resolution, the effects of curved surfaces and roughness levels are not considered in this study. **(2)** Further, the thickness of the material can affect the result of reflectivity. This work only classifies the surface reflections and only considers the reflection from the first interface.

2 Related Work

Material Sensing Using Commodity Devices: Several prior works such as TagScan, LiquID and LiqRay [8, 30, 33] have focused on sensing materials by capturing the changes in wave propagation speed and attenuation through materials, yet remain too bulky and have strict constraints on the container's geometry, thereby limiting their practicality. Other approaches [17, 32, 41] rely on the surface tension, vibration signatures or tracking air bubbles to classify liquids. At the mmWave frequencies, non-contact mmWave vibrometry solutions [13, 18, 29] have detected micrometer-level

	Spectrum	Method	Non-Invasive	Polarimetry	Imaging (Resolution)	Model-based	Material
TagScan [33]	RFID	Penetration	✔	✖	✔ (dm)	✔	Liquids, Solids
LiquID [8]	UWB	Penetration	✔	✖	✖	✔	Liquids
WiMi [10]	WiFi	Penetration	✔	✖	✖	✔	Liquids
LiqRay [30]	WiFi	Penetration	✔	✖	✖	✔	Liquids
LiqDetector [34]	mmWave	Penetration	✔	✖	✖	✔	Liquids
Counterfeit Liq. [32]	Camera	Bubble Movement	✖	✖	N/A	✔	Liquids
PowDew [42]	Camera	Droplet Movement	✖	✖	N/A	✖	Powders
CapCam [41]	Camera	Vibration	✖	✖	N/A	✔	Liquids
Vi-Liquid [17]	IMU	Vibration	✖	✖	N/A	✔	Liquids
RFVibe [29]	mmWave	Vibration	✔	✖	✖	✖	Object-specific
MiLTOn [13]	mmWave	Vibration	✔	✖	✖	✖	Ceramic Cups
RadarCat [40]	mmWave	Range Profile	✔	✖	✖	✖	Object-specific
IntuWition [43]	WiFi	Backscatter	✔	✔	✖	✖	Solids
SiWa [45]	UWB	Backscatter	✔	✔	✔ (cm)	✖	Solids
TagTag [36]	RFID	Normal Reflection	✔	✖	✖	✔	Liquids
mSense [35]	mmWave	Normal Reflection	✔	✖	✖	✔	Object-specific
WiPainter [37]	WiFi	Reflection	✔	✔	✔ (dm) (w/o/ phase)	✔	Solids
POLySight **(Ours)**	mmWave	Reflected SAR at large incident angle	✔	✔	✔ **(2.8 mm)**	✔	**Fine-grained Liquids, Solids, Powders**

Table 1: Comparison of related methods. (Model-based : ✔-physics inspired model was used, ✔-physics constant were calculated)

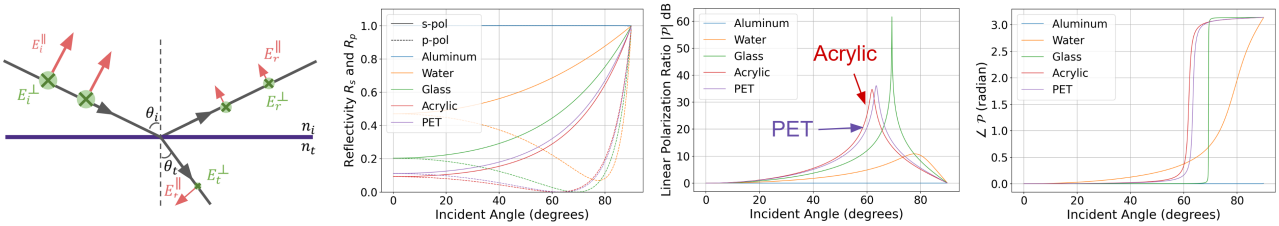

Figure 3: Fresnel simulation of common materials highlighting the increased separation near the materials' Brewster angle

accuracy of vibration, solid material classification as well as detecting breakage. These solutions require active mechanical activation of the object which remains too invasive.

Researchers have also explored classifying liquids [34] and solids [35, 37, 43, 45] using the reflected signals from the objects. IntuWision, SiWa, M-Sense and WiPainter [35, 37, 43, 45] utilize backscattered signals and polarization signatures, but due to limited accuracy and resolution, some of them rely heavily on machine learning, which reduces interpretability and generalizability.

In contrast, POLySight operates on mmWave SAR imaging and polarimetry, enabling millimeter-level spatial resolution and polarization dependent material sensing. POLySight moves the burden of sensing effort from the object or material to the sensor. Hence, our system has no strict geometric constraints and works for both liquids and solids.

Radar Polarimetric Sensing: Radar polarimetry has been used in the remote sensing communities over multiple decades for extracting the scattering coefficients of the earth and has been applied to various areas including climate [31], agriculture [25], and military [7]. Ocean flow, vegetation categories and urban areas can be classified by polarimetry SAR (polSAR) [6, 15]. polSAR was also used in weapon and crack detection [3, 4]. POLySight develops a polSAR at mmWave frequencies taking advantage of higher resolution of imaging for fine-grained material classification. Unlike remote sensing, everyday materials behave differently at 77 GHz as shown in our measurement study in Sec. 3.2. POLySight develops a multi-static imaging solution at mmWave frequencies by measuring these Fresnel reflections.

Bi- and Multi-Static Radar: Around the early 2000s, bi- and multi-static SAR systems were first introduced for military surveillance applications as they are inherently difficult to detect [16]. Later, the first space-based bi-static SAR system, TanDEM-X, was launched for Earth observation and topographic mapping [1, 19]. These prior works operate at small incidence angles by capturing the volumetric reflections of different land types. For commodity devices, multiple-input multiple-output (MIMO) radar has gained significant attention in recent decades due to its ability to achieve higher angular resolution [11]. Further,[44] proposed a scalable phased-MIMO architecture to reduce the cost and improve the scalability, enabling more flexible and accessible MIMO radar deployments.

Unlike prior work, POLySight combines distributed COTS FMCW mmWave radars that are originally designed for mono-static operation to form a multi-static radar system. We achieve

this by intentionally interfering the distributed radars with each other for phase-level synchronization.

3 Polarimetry in mmWave band

3.1 Polarimetry Primer

An incident linearly polarized electromagnetic plane wave $\mathbf{E_i}$ and its reflected wave from the interface $\mathbf{E_r}$ can be expressed as:

$$\mathbf{E_i} = (\mathbf{E_i^p} + \mathbf{E_i^s})e^{j(\mathbf{k_i}-\omega_i t)} \quad \mathbf{E_r} = (\mathbf{E_r^p} + \mathbf{E_r^s})e^{j(\mathbf{k_r}-\omega_i t)} \tag{1}$$

where E_i^p and E_i^s denote the decomposed amplitudes of p-polarization and s-polarization that also keeps track of the phase, subscript s and p denote the direction of polarization, s means perpendicular to the plane of incidence and p denotes parallel to the plane of incidence as illustrated in Fig. 3. $\mathbf{k_i} = k\mathbf{r_i}$ and $\mathbf{k_r} = k\mathbf{r_r}$ are the incident and reflected wave vectors and $k = n\omega/c$, where n is the complex refractive index. According to the Fresnel equation, the reflection coefficient can be calculated as:

$$r_s = \frac{E_r^s}{E_i^s} = \frac{n_i cos\theta_i - n_t cos\theta_t}{n_i cos\theta_i + n_t cos\theta_t} \quad r_p = \frac{E_r^p}{E_i^p} = \frac{n_i cos\theta_t - n_t cos\theta_i}{n_i cos\theta_t + n_t cos\theta_i} \tag{2}$$

Where n_i, n_t are the reflective index of incident and transmitted media, θ_i, θ_t are the incident and transmitted angle respectively. They are related by Snell's Law as $n_i sin\theta_i = n_t sin\theta_t$.

The reflectance of common materials $R_s = |r_s|^2$ and $R_p = |r_p|^2$ are plotted in Fig.3. The incident angle at which the interface has the lowest s-polarization reflectance is called the Brewster's angle. Fig.3(c) shows the ratio of reflectance $\mathcal{P} = r_s/r_p$, as the incident angle increases. As we can observe, the ratio of the reflected power of each polarization increases dramatically near the Brewster's angle [20, 21, 28].

Note that r_s, r_p are both complex amplitude, and the complex reflective index $n = \sqrt{\epsilon\mu} \approx \sqrt{\epsilon}$, since $\mu \approx 1$ because most of the materials are non-magnetic at high frequency [8]. Hence, from the ratio of amplitude orthogonal polarizations $\mathcal{P}$, we can calculate the complex permittivity as [37]:

$$\mathcal{P} = \tan\Phi_{m,\theta_i} e^{j\Delta_{m,\theta_i}} \quad \epsilon = \left(1 + \frac{4\mathcal{P}}{(1-\mathcal{P})^2} sin^2\theta_i\right) tan^2\theta_i \tag{3}$$

3.2 Motivation Study

Given the prior polarimetric remote sensing literature, we first develop a mono-static polarimetric radar system by synchronizing multiple distributed radars (see Sec. 5 for more details) and align them to receive orthogonal s- and p- polarization responses. Our first setup (shown in Fig. 4 (left)) co-locates the transmitting (TX) and receiving (RX) radars looking directly at the object at an incident angle of 0°. As shown in Fig. 4 (top), we can clearly see that the ratios of the polarization for both acrylic and glass surfaces are very close to each other. At first glance, this may seem surprising as the two materials do indeed have different refractive indices. However, there is a fundamental reason behind this unexpected observation.

Thus, we dive deeper and simulate the reflections of multiple different materials at the mmWave frequencies (Fig. 3 (right)), and we observe something that the above physics predicted correctly: **the variation in polarization across materials only expresses itself differently at high incidence angles** (especially close to

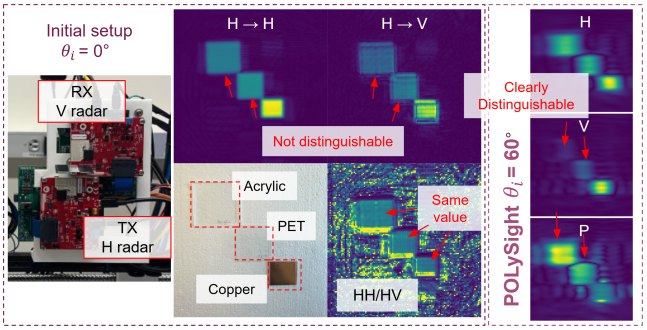

Figure 4: POLySight Motivation Study: We demonstrate that Acrylic and PET are indistinguishable from each other via front-on polarimetric image. The materials express their polarization behavior at high angles of incidence.

Brewster angle). This is indeed validated upon capturing the SAR image of the same materials at a higher incident angle (Fig. 4 (right)), using the testbed in (Fig. 2), where the ratio of the s- and p- polarization images is clearly visible and aligns with our expectation. Further, we notice that **there is a Goldilocks zone between 55° - 65°** where even small changes in permittivity (ϵ' and ϵ'') lead to significant changes in the ratio of the received polarization intensities. Finally, the **benefits of leveraging polarization** are clearly visible in the above example **for classifying the materials**.

These observations indicate, the surfaces of everyday materials are electromagnetically smooth at 77 GHz, causing most of the signal energy to be specularly reflected which follows the Fresnel Equations. Whereas polSAR in remote sensing relies on complex scattering behavior from the Earth's rough surface, which drastically changes polarization and backscatters significant energy towards the transmitter.

4 POLySight System Overview

Our system, POLySight, operates as follows: We use one transmit mmWave radar (rotated by 45°) and two orthogonally placed linearly-polarized receive radars placed along a plane. We transmit the FMCW chirps from the transmitter and receive the reflected signals across both receive radars. This setup is mounted on a 2D motion stage to capture these reflections across a large synthetic aperture. These signals are phase-coherently combined to generate high-resolution complex images describing the accurate reflected behavior along both co-polarized and cross-polarized axes. We then analyze the phase and amplitude ratios of these images to extract the complex permittivity of the surface and classify the objects under consideration. As one would expect, the above design relies on two fundamental contributions in system design to operate in real-time. (1) synchronization of distributed radars and (2) polarimetric imaging and material classification.

Distributed Radar Phase Synchronization: We perform the synchronization across the multiple radars in multiple steps. First, we use a reconfigured hardware trigger to ensure that the signal transmitted is received within the sampling frequency of the radar ADC (Sec. 5.1). We then engineer a direct path between the radars via careful physical calibration and remove fine-grained phase and frequency offsets from the object's reflected signal. Finally, we

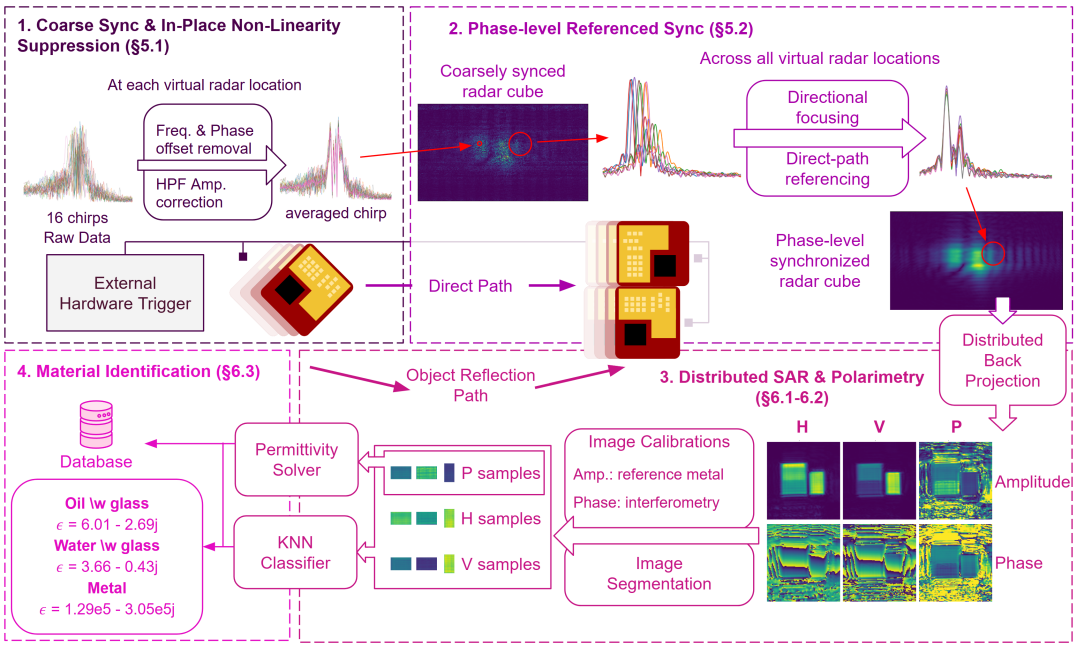

Figure 5: POLYSIGHT **System Overview**

compensate for the non-linear effects caused by the differences in filters and chirp generation to retrieve the denoised signal (Sec. 5.2).

SAR Imaging and Material Classification: We generate the distributed SAR images using back projection (BP) algorithm (Sec. 6.1) for each channel. We then calibrate the images by leveraging a metal reflector and the interferometric natural of distributed SAR. Extract the polarization ratio and phase of the materials and calculate the complex permittivity (Sec. 6.2) shown in Tab. 2. Finally, we show the ability of classifying numerous solid materials using three channels of the SAR images with a simple weighted KNN classifier (Sec. 6.3).

5 Synchronizing distributed mmWave radars

Given the insights developed in Sec. 3, We endeavor to develop a distributed bi-static radar system by synchronizing distributed commodity radars to capture the reflected signal. The first obvious goal is to receive any signal at the RX, then the second goal is to ensure phase-stable channel impulse response.

5.1 Coarse-Level Synchronization for FMCW Reception via Hardware Trigger

Challenge: At first glance, the first challenge of capturing a signal at the receiver feels trivial. A näive solution would transmit the FMCW chirps continuously expecting to see a received signal at the receiver radar. However, this is simply not true. The explanation of this surprising phenomenon lies in how the commodity FMCW radars sample the signal.

A traditional radar transmits a FMCW signal expressed by $s_t(t)$ where the received reflected signal $\hat{s_t}(t)$ is a delayed version of the transmitted signal.

$$s_t(t) = e^{j2\pi(f_0 t + 0.5Kt^2)} \qquad \hat{s_t}(t) = \sigma e^{j2\pi(f_0(t-\tau)+0.5K(t-\tau)^2))}$$

In this example, σ is the radar cross section of the reflector, $\tau = 2d/c$, is the round trip delay of the reflector at distance d and speed of light c. The received signal will be passed to the mixer that multiplies the original transmitted signal with the received signal. The produced signal is called intermediate frequency (IF) signal and can be expressed as: $s(t) = \sigma e^{j2\pi(K\tau t + f_0\tau - 0.5K\tau^2)}$. The last term $0.5K\tau^2$ is called residual video phase (RVP) and is normally ignored [39]. The IF signal is a monotone complex exponential with frequency $K\tau$ and phase $2\pi f_0\tau$. This signal is then sampled at a sampling rate of around 10 MHz (much smaller than the 5 GHz bandwidth) to identify the power-delay profile of the received signal. Further, hardware filters block signal outside this maximum sampling rate to avoid aliasing of far-away reflectors.

This means that any received chirp received at delay of more than 0.257 μs out of a total chirp duration of 128.5 μs will go completely unnoticed by the receiver. Thus, there will be a 0.2% chance of any transmitted signal being visible at the receiver. Hence, it is required to ensure that the additional random delay added due to lack of synchronization between the transmitter and receiver must be smaller than $0.257\mu s$ given the slope of our chirp.

Hardware-Trigger based Coarse Synchronization: At first glance, the obvious solution would be to share the analog clock between the transmitter and receiver. However, most commodity mmWave radars[1] do not provide an analog OCXO I/O. However, there is a mechanism that all TI mmWave radars expose that can address our problem to an extent, that is the hardware trigger.

Specifically, we can enable simultaneous triggering of both the transmitter and receiver radars by mapping the start of operation to the rising edge of a 1 MHz square wave. However, remember that while the triggering ensures that the transmitted signal and

[1]While most of our discussion revolves around TI mmWave radars, the assumptions are true for all commodity FMCW mmWave radars

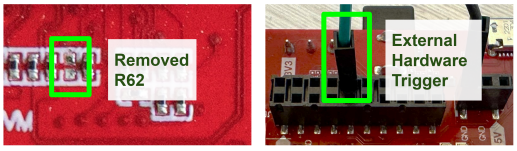

Figure 6: To enable the SYNC_IN signal from an external source through pin 16, resistor R62 must be removed.

receiver signals are generated at the same time, each of these signals are generated by two different local oscillators. While these low-frequency oscillators are typically good quality and very accurate, the significant upconversion required to reach mmWave frequency bands significantly amplify their residual frequency and timing offsets due to factors such as temperature. However, these residuals remain small enough to ensure guaranteed reception of signals at the receiver mmWave radar.

On commodity evaluation modules made available by TI, these hardware triggers are explicitly blocked by a resistor and need to be enabled by removing this blocking resistor from the evaluation modules as shown in Fig. 6.

5.2 Fine-grained Synchronization of FMCW Radars via Direct Path Reference

While the above coarse-grained synchronization ensures reception of the signal, it fails to achieve time and phase coherency of the received signal across virtual antennas. Specifically, the received signal for each chirp at the receiver can be written as follows:

$$s'(t) = s(t)e^{j(2\pi\Delta f t + \Delta\phi)} \tag{4}$$

These phase ($\Delta\phi$) and frequency offsets (Δf) need to be removed to achieve phase-synchronized reception for extracting accurate material polarization phase and amplitude, as well as, imaging the scene accurately using synthetic aperture radar (SAR). This is further complicated by the fact that these offsets change for every single chirp as they are generated from the clock noise. Thus, there is a need for a solution that can remove these offsets on a per-chirp basis for phase extraction and imaging.

Our solution to this remarkably difficult challenge relies on an important insight: the offsets affect all reflected paths equally within the chirp. Thus, let's say we augment a reference object with a known radar cross section (σ_{ref}) and time-of-flight (τ_{ref}) in the environment, then the received signal can be written as:

$$s'(t) = [\sigma e^{j2\pi(K\tau t + f_0\tau)} + \sigma_{ref} e^{j2\pi(K\tau_{ref} t + f_0\tau_{ref})}]e^{j(2\pi\Delta f t + \Delta\phi)} \tag{5}$$

Thus, assuming the τ_{ref} is significantly different from the actual τ, we can extract the reference signal behavior to identify the offsets (Δf and $\Delta\phi$) and then compensate for them to retrieve the true received signal $s(t)$ from $s'(t)$. However, ***adding an actual known reference reflector in perfect orientation is unreasonable in every possible passive sensing scenario and cannot be practically augmented***. However, there does exist one path between the transmitter and receiver that always exists and can be leveraged to compensate for the above offsets: the direct path.

Engineering the direct path: The standard SAR imaging solution would place the mmWave radar directly facing the object to maximize the energy reflected by the object. However, in our bi-static and polarimetric imaging setting, the TX and RX radars need to be placed differently to ensure a coverage of both the object and the direct visibility between radars. Moreover, the amplitude of direct path and object path needs to be balanced for precise synchronization and accurate reconstruction. Further complicating the design is the goal of receiving both co- and cross-polarizations. Thus, first, the TX is placed with 45° tilt angle to ensure equal energy on s- and p-polarizations. Second, given the azimuth coverage of the antenna is about 120°, TX and RX are placed facing towards each other in the horizontal plane. Finally, the cross polarized RX radar has an additional 20° horizontal angle to compensate for the narrow elevation coverage of the receiver antenna.

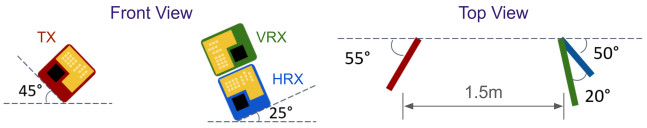

Figure 7: POLySIGHT radar placement

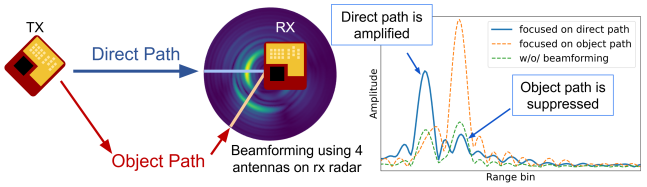

Figure 8: Use beamforming at receiving radar to increase the SNR for synchronization

Next, to further achieve higher SNR and improve the accuracy of frequency and phase compensation, the receiving radars perform beamforming to separate the direct path and reflection from the object given that 4 RX chains are naturally synchronized on the same radar. This operation significantly amplifies the direct path as shown in Fig. 8. After isolating the direct path, frequency and phase compensation factors are found at the peak value. Hence, the random time delay between signals at different locations can be removed and the range profiles are synchronized by referencing to the direct path. Note that, the whole RX module is tilted 25° for better horizontal beamforming resolution.

We carefully calibrate our system using a metal square reflector to explore different angles of reception to ensure the optimal trade-off between the reception of direct path, coverage of the imaging system and maximizing the SNR of the imaged object reflection. Our final optimal design is illustrated in Fig. 7.

Dealing with chirp non-linearity and high-pass filter hardware effects: While the above solution, deals with all linear frequency and phase offsets that dominate the reflected signal, there are three particular effects of the mmWave radar that need to be further addressed. The first non-linear effect originates from the ramp-up and ramp-stop stages of the chirp, where a ripple effect is caused by the sudden frequency changes. Given the distributed nature of POLySIGHT's setup, these non-linear behaviors between separate radars are very distinct and it can significantly affect the phase and amplitude of the IF signal as shown in Fig. 9. Thus, our synchronization approach only utilizes the central half of the chirp which is mostly linear.

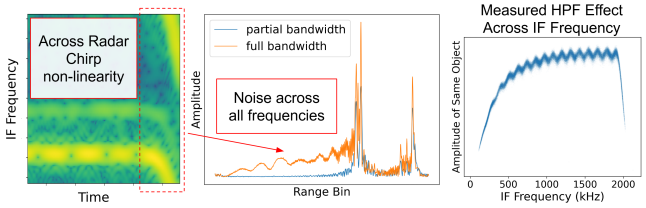

Figure 9: Across Radar Non-linearity Analysis. (left) Spectrogram of across radar received IF signal where chirp non-linearity exist. (center) The noise effect across all frequencies if we use full-bandwidth. (right) The measured HPF induced and IF frequency dependent amplitude bias.

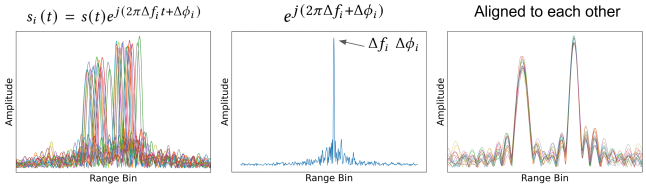

Figure 10: In place (at each virtual antenna location) synchronization for suppressing chirp non-linearity. The aligned chirps are coherently averaged before fine-grained synchronization.

Additionally, even the center part of the chirp is not perfectly linear which becomes noise across all frequencies in the IF signal after mixing. We solve this by coherently taking average of 16 chirps at each virtual antenna location. However, since the random frequency and phase offset exists for every chirp, we first synchronize chirps captured at the same location. Since those chirps are collected at exactly the same scene, they are randomly delayed versions of each other just like Equation 4. Given 2 offset signals $s_1(t) = s(t)e^{j(2\pi\Delta f_1 t+\Delta\phi_1)}$ and $s_2(t) = s(t)e^{j(2\pi\Delta f_2 t+\Delta\phi_2)}$, the division is a complex exponential carrying their frequency and phase difference. The compensating factor can be found from the peak value of the Fourier transform of that signal. We can then rotate the signal by $s_2'(t) = s_2(t)e^{j(2\pi(\Delta f_1-\Delta f_2)+\Delta\phi_1-\Delta\phi_2)}$ which aligns them to each other. We illustrate this process in Fig. 10.

Another effect is that of the high-pass filter (HPF) applied on the signal on the mmWave radars to remove on-chip interference. As shown in Fig. 9 (right), the filter removes the low-frequency response (the on-chip strong signal leakage) in the sampled IF signal at the receiver. This high-pass filter is applied to avoid saturating the ADCs at the receiver chain and cannot be disabled. Unfortunately, this filter has an erratic amplitude response even at higher frequencies affecting the amplitude of the received signals.

We first measure this frequency dependent HPF effect by adjusting the starting frequency of the receiving radar in a fine-grained manner. As the range profile moves across IF bandwidth, we then record the amplitude of the same reflector at different IF frequencies. Finally, we model the HPF effect as an LCCDE filter to compensate for these amplitude variations. The modeled HPF effect is shown in the right of Fig. 9.

Our results in Sec. 9.1 demonstrate that those steps significantly amplify the phase and frequency offset correction stability of our measurements. Those techniques enable us to capture the accurate amplitude ratios across the two radars where the transmitted signal

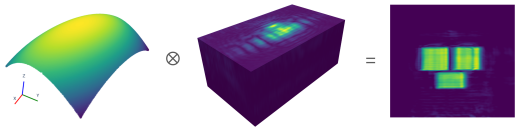

Figure 11: Distributed SAR generation after synchronization

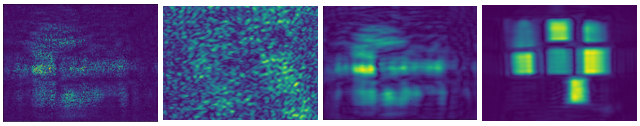

Figure 12: The effect of unsynchronized IF signal in reconstructing SAR images. From left to right: (a) coarsely synchronized radar cube and (b) its corresponding generated SAR image. (c) phase-level synchronized radar cube and (d) its corresponding reconstructed SAR image.

is received at different times due to time-of-flight and synchronization delays. Note that this compensation is applied prior to the fine-grained synchronization as the direct path is also affected by these erratic amplitude behaviors. We thus end with a synchronized phase and amplitude measurement across two paths: one co-polarized and one cross-polarized. The standard deviation of the frequency around the correct frequency after synchronization is 138 Hz (as shown in Sec. 9.1).

6 Imaging and Identifying Materials

In this section, we leverage the distributed synchronized bistatic polarimetric imaging deployment to image and categorize materials.

6.1 Distributed SAR Imaging

Our system uses Back Projection (BP) algorithm that applies matched filters to each antenna pair for SAR reconstruction. For a voxel $r = (x, y, z)$ in space, the received signal $s(r)$ can be calculated as [9]:

$$\mathbf{s}(\mathbf{r}) = \sum_{i=0}^{A}\sum_{n=1}^{N} S_i(n)e^{j2\pi d_v^i(f_0+kn)/c} \tag{6}$$

Where A and N are the number of synthesized antennas and number of samples in each chirp, $S_i(n)$ is the FFT of signal $s_i(t)$ at $i-th$ synthesized radar location. d_v^i is the total distance signal traveled from the transmitter location p_i^{tx} to the object v and arrived at the receiver p_i^{rx}. Different from conventional mono-static settings that $d_v^i = d(v, p_i^{tx}) + d(v, p_i^{rx}) \approx 2 \times d(v, (p_i^{tx} + p_i^{rx})/2)$, the distances for our bi-static setting are all relative distances since our system synchronizes the chirps by referencing to the direct path. Hence, the distance of direct path should be removed from every calculated distance $d_v^i = d(v, p_i^{tx}) + d(v, p_i^{rx}) - d(p_i^{tx}, p_i^{rx})$. Since virtual radar points are evenly sampled in space, the BP calculation for one voxel can be interpreted as matrix multiplication between the radar cube and the point spread function (PSF). Extending from one voxel to the entire imaging plane, the reconstruction process is a convolution between the radar cube and the PSF, as illustrated in Fig. 11.

Fig. 12 illustrates an example of the FFT cube with coarse-level and fine-grained phase-level synchronization, and the corresponding reconstructed SAR images. Without fine-grained synchronization, the frequency misalignment across 2D makes it impossible to reconstruct the SAR image. In contrast, after applying phase-level

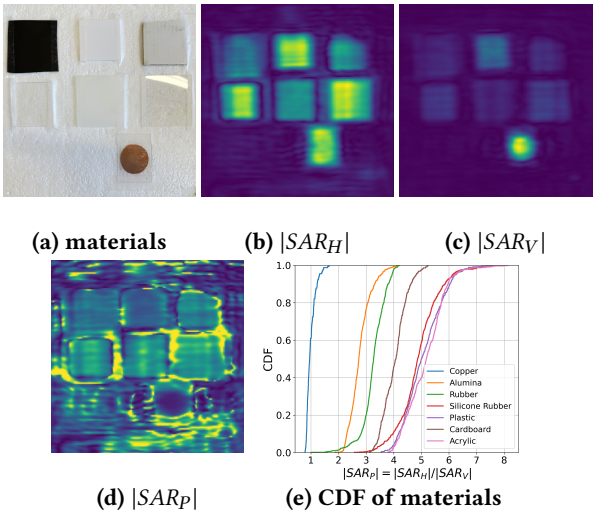

Figure 13: SAR collected at $\theta_i = 50°$. Materials from upper left to lower right are: rubber, Alumina, cardboard, acrylic, silicone rubber, plastic, and a circular copper tape stacked on square plastic

synchronization, the FFT cube exhibits coherence, resulting in a well-focused and high-resolution SAR image.

Spatial resolution: Since the reflected path in our system can be interpreted as backscattered back to the transmitter, which is the same as conventional SAR imaging. The spatial resolution of our system can be approximately calculated using the same equation $\delta = r * \lambda/L$ [12], where r is the distance from radar to the imaging plane, λ is the wavelength, and L is the effective antenna dimension along the azimuth direction. Since our system synthesized an aperture size of 40 cm × 70 cm. For imaging plane 50 cm away from SAR virtual array plane ($\theta_i \approx 55°$), the spatial resolution of POLySight is 4.9 mm × 2.8 mm.

6.2 Amplitude and Phase Calibration via Interferometry

We require both phase and amplitude to extract the permittivity from the ratio of the HRX and VRX SAR channels. Nevertheless, the SAR images of two channels still face several issues and need careful calibration. The first challenge comes from the nature of SAR images, the phase of each pixel is both related to the distance that signals traveled and the reflection from the material [22]. Since reflection-induced phase change is very subtle (Fig. 3 (right)), it can be easily overwhelmed by the distance-induced phase that spans across 2π for every wavelength. Further, the synchronization relies on a precise distance of the direct path. However, the direct distance is manually measured and has sub-mm error, which may cause constant phase offsets for SAR images. Another issue is, the amplitude is unbalanced as radars have separate ADCs and also the 25° tilt angle of RX radars mentioned in Sec. 5.2. POLySight first calibrates the phase with the following insight: **distributed**

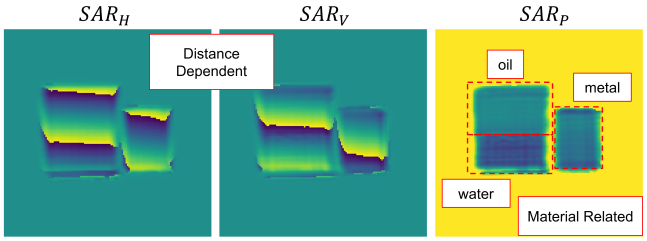

Figure 14: Phase of each SAR channel

(multi-static) radar setting enables not only polarimetry but also interferometry. Mathematically:

$$\mathbf{s}^P_{m,\theta_i}(\mathbf{r}) = \frac{|\mathbf{s}^H_m(\mathbf{r})|}{|\mathbf{s}^V_m(\mathbf{r})|} e^{j\left((\Delta^H_{m,\theta_i} - \Delta^V_{m,\theta_i}) + (\varphi^H(\mathbf{r}) - \varphi^V(\mathbf{r})) + (\varphi^H - \varphi^V)\right)}$$

The H, V represent the SAR image channels from TX to HRX and VRX respectively, and P represents the ratio of H and V channels. $\mathbf{s}^H_m(\mathbf{r})$, $\mathbf{s}^V_m(\mathbf{r})$, $\mathbf{s}^P_{m,\theta_i}(\mathbf{r})$ are complex values of H, V and P SAR image channels. Δ^H_{m,θ_i}, Δ^V_{m,θ_i} are reflection-induced phase changes of H and V channels for material m at incident angle θ_i. $\varphi^H(\mathbf{r})$, $\varphi^V(\mathbf{r})$ are distance-induced phase changes of H and V channels. φ^H and φ^V are constant phase offsets of H and V channels. Note that, H channel captures the s polarization and V channel captures the p polarization. Hence, the $\mathbf{s}^P(\mathbf{r})$ represent the polarization ratio mentioned in Sec. 3. Let $\Delta_{m,\theta_i} = \Delta^H_{m,\theta_i} - \Delta^V_{m,\theta_i}$ which is material related phase change at incident angle θ_i. Since the relative locations of radars and the imaging plane are fixed, the difference of distance-induced phase change is also constant. Let this constant offset to be $\varphi^{H,V} = (\varphi^H(\mathbf{r}) - \varphi^V(\mathbf{r})) + (\varphi^H - \varphi^V)$. The complex value at $\mathbf{r}$ can be written as:

$$\mathbf{s}^P_{m,\theta_i}(\mathbf{r}) = |\mathbf{s}^P_{m,\theta_i}(\mathbf{r})| e^{j(\Delta_{m,\theta_i} + \varphi^{H,V})} \tag{7}$$

As shown in Fig. 14 (areas outside the target are masked), the target is water and oil inside the same square container. We can see that the phase of H and V channels is unstable since targets are not perfectly parallel to the SAR collection plane and the phase of reflection is totally overwhelmed. However, as Eq.7 shows, the P channel shows a clear difference between water, oil and metal. Thus, the phase induced by reflection is extracted by interferometry.

Next, we try to deal with the remaining $\varphi^{H,V}$ and the unbalanced amplitude. Let Φ_{m,θ_i} be the polarization ratio of material m at incident angle θ_i, then $|\mathbf{s}^P_{m,\theta_i}(\mathbf{r})| = \alpha_{H,V} \tan \Phi_{m,\theta_i}$, and $\alpha_{H,V}$ is a scalar denoting the amplitude ratio offset between H and V SAR images. From Sec. 3 we plotted that since conductive materials like metal have nearly infinite permittivity at mmWave frequencies, signals will be fully reflected despite the polarization state. So, given a signal with the same amount of energy on both orthogonal polarizations, the reflected energy of both polarization should be the same. That is $\Phi_{metal,\theta_i} = 45°$ and $\tan \Phi_{metal,\theta_i} = \tan 45° = 1$. Moreover, the phase of the polarization ratio remains $\Delta_{metal,\theta_i} = 0$ until 90° incident angle. For a metal object located at $\mathbf{r}'$, the permittivity can be calculated using Eq. 3.

$$\mathbf{s}^P_{metal,\theta_i}(\mathbf{r}') = \alpha_{H,V} \tan \Phi_{metal,\theta_i} e^{j(\Delta_{metal,\theta_i} + \varphi^{H,V})}$$

Hence, metal can be used as a known reference object for correcting both amplitude and phase:

$$\Phi_{m,\theta_i} = \arctan\left|\frac{\mathbf{s}^P_{m,\theta_i}(\mathbf{r})}{\mathbf{s}^P_{metal,\theta_i}(\mathbf{r}')}\right| \quad \Delta_{m,\theta_i} = \angle\left(\frac{\mathbf{s}^P_{m,\theta_i}(\mathbf{r})}{\mathbf{s}^P_{metal,\theta_i}(\mathbf{r}')}\right) \quad (8)$$

6.3 Material Characterization and Classification

Given the corrected polarization ratio Φ_{m,θ_i} and phase Δ_{m,θ_i}, the permittivity can be calculated using Eq. 3. Our permittivity estimates for 36 materials are listed in Sec. 9.2

Beyond characterization, POLySight also enables classification of unknown materials. Directly classify using estimated complex permittivity is straightforward but failed to leverage the advantage of polarimetry. To fully utilized the enhanced contrast between materials, we use the calibrated value of all 3 channels H, V and P as feature vectors and use KNN model for classification according tot he previous collected dataset. Given SAR images of H, V and P channels, We first segment materials into patches, then calibrate the material vector using the averaged metal vector.

$$\bar{\mathbf{s}}_{metal,\theta_i} = \frac{1}{N}\sum_{r'\in A}\mathbf{s}_{metal,\theta_i}(r') \quad \tilde{\mathbf{s}}_{m,\theta_i}(\mathbf{r}) = \frac{\mathbf{s}_{m,\theta_i}(\mathbf{r})}{\bar{\mathbf{s}}_{metal,\theta_i}} \quad (9)$$

Where A is the metal area, and $\tilde{\mathbf{s}}_{m,\theta_i}(\mathbf{r})$ is the calibrated material vector at location r that has three elements of H, V and P channels. Note that, this calibration is necessary since the gain of radars will vary for each power cycle. Then the distance for the KNN classifier is a weighted sum with three hyperparameters λ_H, λ_V and λ_P as the weight for each channel. Since the phase in H and V channels are not related to materials, only the absolute values are used. Although most of the materials can be differentiated at a high incident angle (e.g. 60°), multiple incident angles can be used for getting richer features and combined for classification. We have discussed the effect of θ_i for classification in Sec. 9.1 and extensively evaluated the fine-grained classification ability of POLySight in Sec. 9.3.

7 Discussions and Limitations

While POLySight is the first reflection polarimetry-based material detection solution at the mmWave frequencies, there are several limitations in our work that can be addressed in the future.

Reflections off mostly flat surfaces: Our solution assumes that the reflections are primarily coming off surfaces which can be considered flat relative to the wavelength. The real world is full of objects in many shapes (curves, sharp edges) and forms (small and large) and even rough surfaces (brittle, spiky) which need to be appropriately handled in a future work in a similar vein to the same challenges in object identification in non-line-of-sight scenarios [9].

Thickness of materials: Currently our system only consider single layer reflection. However, as mmWave signals penetrate, the multiple interface reflection is usually inevitable. Especially for solid objects with low permittivity, the reflection on the second interface can affect the estimation result. This is the reason why we have analyzed several materials with different thicknesses. Also, as liquids in our experiments are stored in glass containers, the reflected signal is a combined feature of glass and liquid. Future work can be solve this by using multi-interface model or learning based methods.

Slow scanning: Currently, it takes 2 hours for our system to complete the scanning. The main bottleneck is the large aperture required in the bi-static setting. In the future, even more radars can be added into the system to form a larger physical aperture, which can dramatically reduce the scanning steps and shrink the time to a few minutes. Alternatively, accurate SAR reconstruction using sparse array is also a direction to explore.

Machine learning integration: We believe machine learning models would be very helpful for modeling more complex, irregularly shaped objects, which potentially can make the system even more robust and generalizable in real-world environments. Additionally, exploring the combination of RF modality with vision models could potentially help address the lack of data at mmWave frequencies, which is also an interesting direction to explore.

8 Implementation

As shown in Fig. 2, we implement our system using three TI AWR2243BOOST FMCW mmWave radars operating at 76-81 GHz. One radar on the left side serves as the transmitter, while two radars on the right side act as receivers, positioned orthogonally to capture s- and p-polarized reflections. More specific radar placement is also shown in the figure. The copper shield is mounted for preventing back reflection. All radar modules are connected to a Raspberry Pi 3B through their hardware trigger ports. The whole distributed radar module is mounted on a 2D motion stage. The motion stage is controlled by an Arduino UNO board, which is also connected to the Raspberry Pi. The Arduino sends a trigger signal to the Raspberry Pi for every capture. The Raspberry Pi generates and transmits 16 continuous trigger pulses simultaneously to all radar modules. Once triggered, the radars capture the reflected signals and stream the data to the host computer. The synthesized aperture is 40 cm × 70 cm large with a step size of 2 mm for high resolution and balanced gain across the imaging plane. The motor moves at a speed of 20 mm/s and the setup collects 200 × 350 locations within 2 hrs. The distance between TX to RX radars is manually measured. Small position errors have negligible effect on the imaging result and can be corrected as mentioned in Sec. 6.2.

9 Evaluation

9.1 Microbenchmarks

SAR Phase-Level Synchronization Error Analysis. There are 3 kinds of errors during synchronization: frequency, phase, and amplitude. All of those can cause offsets which are extremely harmful for SAR imaging result. We evaluate the quality of synchronization by collecting 640,000 chirps of the same scene using the distributed radar setup. We simplified the scene with a single strong object peak using a metal reflector, then synchronized chirps using different stages of the method introduced in Sec. 5. The distributions of frequency, amplitude and phase offsets are plotted in Fig. 15.

Using all 4 stages, the standard deviation of frequency offset of the IF signal is 0.138 KHz and standard deviation of measured phase of the object peak is 0.022 radian (i.e. about 0.35% of the wave length, which is $4.31 \times 10^{-14}s$ at 80 GHz). Fig.12 (a) and (b) are the SAR image generated only by using coarse hardware triggering. (c)

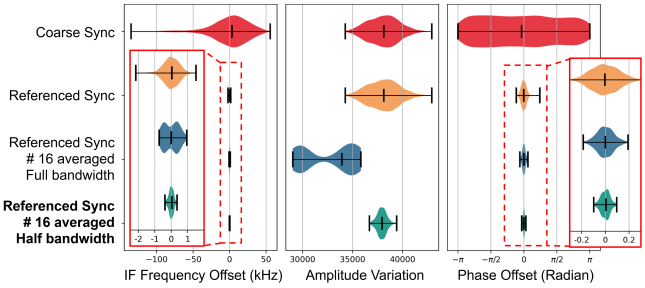

Figure 15: Error Analysis of Stages of Synchronization

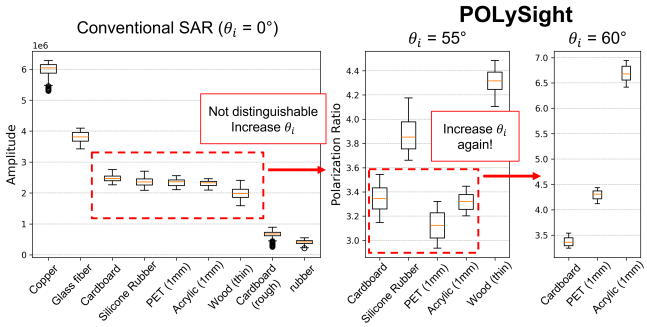

Figure 16: Material contrast across incident angles

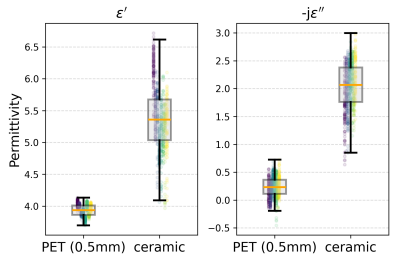

Figure 17: The estimated permittivity of PET and ceramic shows location independence of POLySight**.**

and (d) use all 4 stages of phase-level synchronization and a clear and accurate SAR image can be generated.

Fine-grained material recognition through multiple incident angle. To show that our method can achieve fine-grained material sensing compared to conventional mono-static SAR method ($\theta_i = 0°$), we have collected some conventional images with different materials and plotted their amplitudes in Fig. 16 (left). As the figure shows, only materials with distinct differences like copper, rubber, glass fiber can be directly distinguished, the rest of the materials have the same behavior at 0 incident angle. By using POLySight with $\theta_i = 55°$, we imaged those indistinguishable materials and plotted the polarization ratio in Fig. 16 (middle). The contrast between some materials is enlarged, but, cardboard PET and acrylic are still cluttered since they have highly similar permittivity values. We then increase the incident angle again to $\theta_i = 60°$ which is closer to acrylic's Brewster's angle shown in Fig. 16 (right). They are then clearly distinguishable from the polarization ratio. We further applied this phenomenon for fine-grained classification and quantitatively analyzed it in Sec. 9.3.

Location Independence of POLySight**:** Imbalanced aperture and speckles are common in the SAR images which can variate the value of each pixel [23]. The phase and amplitude errors during synchronization, though very small, could also be harmful for the generated SAR image. Those errors can cause an uneven gain across the SAR image, making the value of each pixel location dependent.

POLySight ensures a balanced gain across the whole image by increasing the synthetic aperture size to 40 cm × 70 cm. With the large imaging plane spanning 15 cm × 15 cm, a 2D gaussian filter is applied to the generated SAR images to reduce speckles. We demonstrate this balanced gain by evaluating POLySight with 8 sets of SAR images with copper, ceramic, and plastic. Each time, those material patches are randomly placed on the imaging surface. We manually segmented the materials and calculated the permittivity of each pixel shown in Fig. 17. The estimated permittivity is scattered with different colors. The variance of the real part ϵ' is 0.0021, 0.0295 for PET and ceramic respectively. The variance of the imaginary part ϵ'' is 0.0255 and 0.1081 respectively, showing the location-agnostic nature of the system.

Materials	ϵ'	$-j\epsilon''$
1. Metal	1.29e5	3.05e5
2. Acrylic (1 mm)	3.56	0.18
3. Acrylic (3 mm)	4.00	0.40
4. Polycarbonate (1 mm)	4.26	0.21
5. PET (0.5 mm)	3.78	0.70
6. PET (1 mm)	3.83	0.73
7. Vinyl (0.37 mm)	3.65	0.70
8. PVC	4.15	0.81
9. PLA (ender, 1 mm)	3.79	0.34
10. PLA (hyper, 1 mm)	4.21	0.30
11. TPU (1 mm)	3.91	0.21
12. Ceramic	4.75	2.43
13. Rubber	5.06	1.11
14. Silicone Rubber	3.52	0.82
15. Glass (2 mm)	7.26	0.85
16. Glass Fiber	4.69	0.70
17. Paper (smooth)	4.63	0.31
18. Cardboard	5.24	0.01
19. Cardboard (rough)	4.54	0.56
20. Fabric	2.21	0.13
21. Wood (thin, smooth)	2.61	0.71
22. Wood (rough)	5.02	0.81
23. Cork	10.6	N/A
24. Soy Sauce (\w glass)	4.30	0.53
25. Corn Oil (\w glass)	6.01	2.69
26. Corn Syrup (\w glass)	6.42	0.05
27. Water (\w glass)	3.66	0.43
28. Cane Sugar (1.3%, \w glass)	3.72	0.43
29. Cane Sugar (3.8%, \w glass)	3.78	0.44
30. Cane Sugar (5.1%, \w glass)	3.81	0.43
31. Cane Sugar (6.3%, \w glass)	3.89	0.41
32. Cane Sugar (7.4%, \w glass)	3.96	0.39
33. Sugar Powder (\w plastic)	4.46	0.42
34. Salt (\w plastic)	4.30	0.94
35. Protein Powder (\w plastic)	5.74	0.45
36. Milk Powder (\w plastic)	4.88	0.74

Table 2: Estimated Permittivity at 76-81 GHz

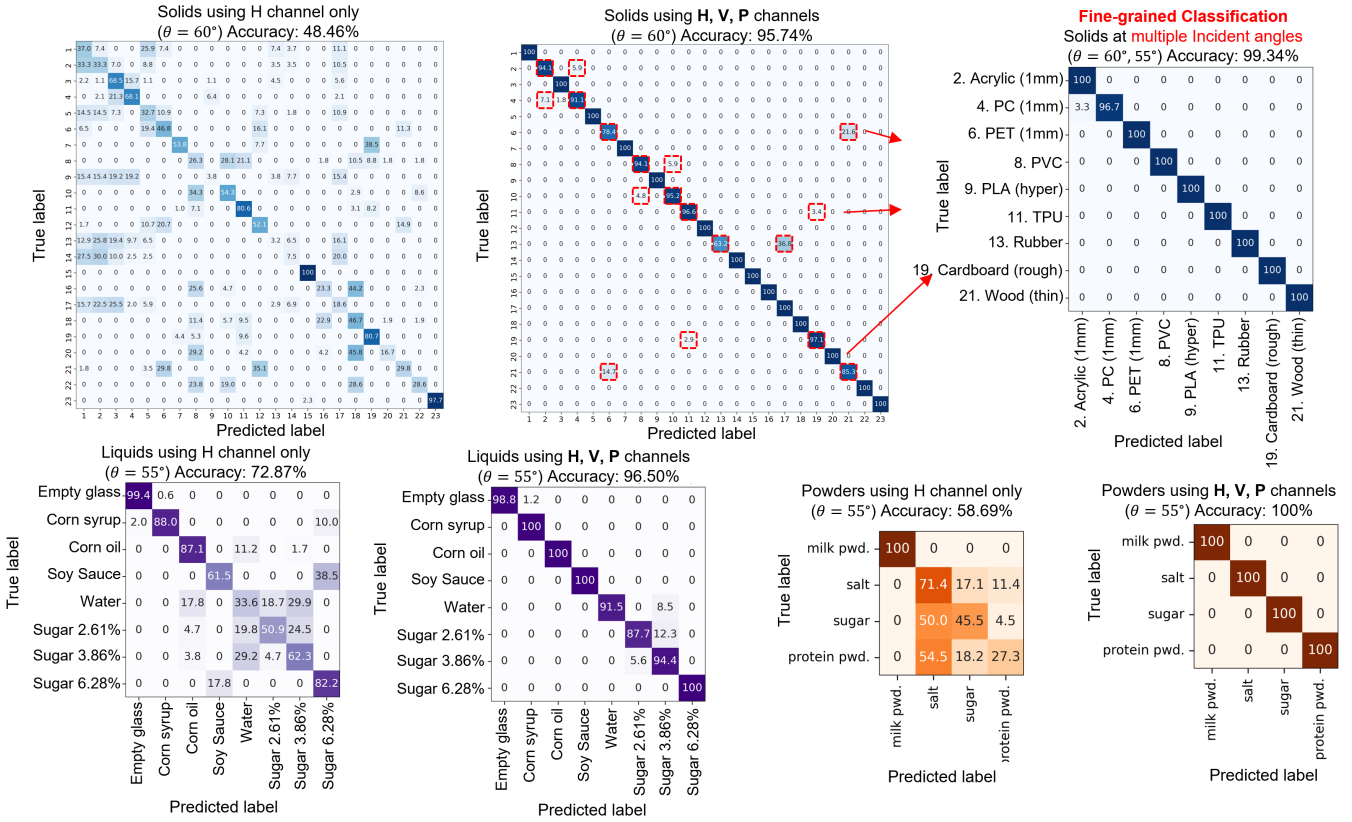

Figure 18: Confusion matrices of pixel-wise material classification : (index of solids corresponds to Tab.2).(top) POLYSIGHT **achieves a classification accuracy of 95.74% across 23 solids by extracting polarization from one angle of incidence and improved from 48.46% of only using H channel for classification. It further improves this to 99.34% by capturing another angle of incidence. (bottom left)** POLYSIGHT **achieves a 96.50% accuracy in classifying 8 liquids improving from 72.87% without polarimetry. (bottom right)** POLYSIGHT **also perfectly classifies 4 different types of powders based on their polarimetric response.**

9.2 Permittivity Estimation

The permittivity is calculated using Equation 3 for each pixel of the calibrated SAR images and averaged for each of the segmented materials and are listed in Tab.2. Solid materials are mounted on a plastic foam which is transparent under mmWave. Liquids are held in glass containers and powders are stored in plastic boxes. Consequently, we notice that the estimated values for liquids are off from the baseline value of water that is about 9.37 for ϵ' and 18.00 for ϵ'' at room temperature of 75 GHz reported in previous literature [24, 27]. That's because the air-glass-liquid interface does not satisfy the single interface assumption of Eq. 3.

9.3 Material Classification

Setup: We place the above mentioned materials in the imaging zone of POLYSIGHT to capture the HH and HV responses similar to Sec. 6. We then use the approach described and the KNN model in Sec. 6.3 to classify the materials. Number of pixels extracted for each material is about 80-120. We compare the classification results of POLYSIGHT with only using the HH response to classify the materials to demonstrate the benefit of leveraging polarization.

Quantitative Benefit: We leverage these measurements (H, V and the ratio P) to classify the solids, liquids and powders. As our results in Fig. 18 clearly show, the classification accuracy increases from 48.46%, 72.87% and 58.69% using just the horizontal polarization response to 95.74%, 96.50% and 100% using all the three measurements. The top row of Fig. 18 shows how many solids such as A and B are completely confused with each other, yet neatly separable using polarimetry. Further, if we capture the response at multiple incident angles, this classification accuracy further improves as shown in Fig. 18 (top right). The liquids are classified using a smaller incident angle (55° vs. 60°) and our system still performs very well and can even classify small changes in concentration of sugar in water accurately (Fig. 21 bottom left).

We also evaluate powders which are especially difficult to classify due to the comparable size of particles to that of wavelength at the mmWave radar frequency bands. This typically leads to spurious multi-reflections and scattering effects corrupting the accuracy of material classification. However, given the large incident angle of POLYSIGHT's system design, these spurious reflections are spread too weak to be received by the receiver enabling POLYSIGHT to correctly predict the various powders (Fig. 18 bottom right).

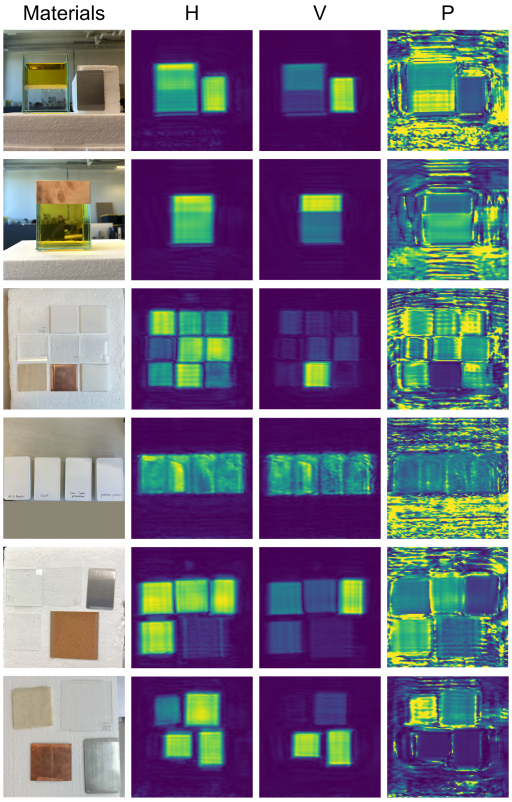

Figure 19: Qualitative Results

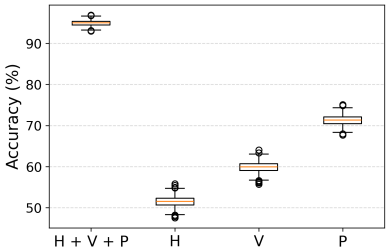

Figure 20: Ablation Study of mmWave Polarimetry

Qualitative Benefit: We first demonstrate a few example images (Fig. 19) of solids, liquids and powders along with the images generated via SAR on the horizontal (H) and vertical (V) receivers as well as the amplitude of ratio (P). As one can clearly see, there are many materials that demonstrate similar horizontal or vertical responses, but can be clearly differentiated by the amplitude and phase of the ratio. For instance, in the third row, we can see that metal is no longer the strongest reflector anymore in our setting since the polarization angle Φ of most of the materials changed. So that in H channel, their amplitude is even higher than that of the metal. Another example is transparent materials, which are indistinguishable using visual cameras and even conventional mmWave SAR imaging, as previously listed in Fig. 16. In our setting, it's much easier to differentiate them in the P channel. These examples demonstrate a qualitative backing to the benefits of leveraging polarimetry for material classification.

Benefits of Polarimetry: Finally, we evaluate the impact of each of the components in classifying the materials. We compare the improvement provided by leveraging all the three components vs. each component individually. Our results in Fig. 20 show that the ratio (P) of the horizontal to vertical shows the best individual classification accuracy. However, POLySight's approach of using all the three components clearly achieves the maximum mean accuracy of 94.93% compared to 51.50%, 59.85% and 71.29% of H, V, and P components respectively.

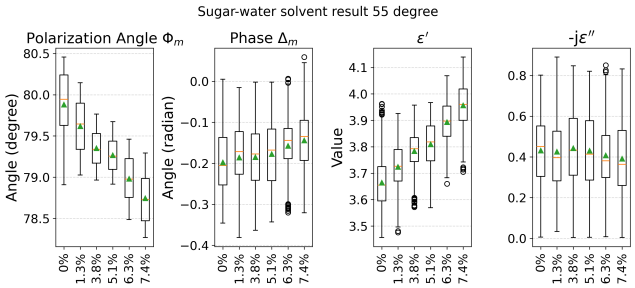

(a) Extracting phase from liquid reflection

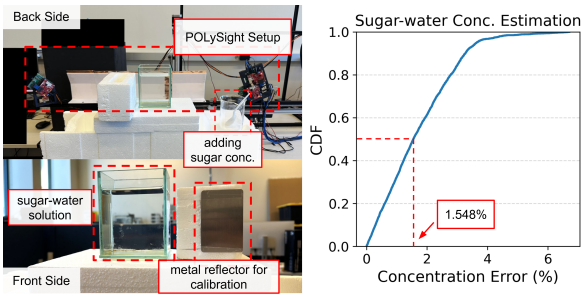

(b) Setup and CDF of estimated error

Figure 21: Case study for liquid concentration estimation

9.4 Case Study on Sugar Concentration

Setup: We test the limits of POLySight by exploring an important problem in many domains on detecting the concentration of a solute in a solvent. Specifically, we take a simple example of dissolving sugar in water and identifying the concentration of the dissolved sugar as % by weight. We first fill our glass beaker with 650 ml of water. Then we keep adding one tablespoon of sugar after measuring its weight one by one to the water and stirring until dissolution. We then capture the H and V responses of the signal reflected from this solution and measure various material characteristics.

Results: Our experimentation setup and results are shown in Fig. 21. As one can clearly see, as the concentration of the dissolved sugar increases, we see a steady decline in the polarization angle and a steady increase in the real permittivity. This shows the ability of the polarization angle and permittivity to sense even small changes in concentration of the liquid. We further use a linear regression model to estimate the sugar concentration of the solution and are able to predict with a median 1.548% error in estimating the concentration of the solution. The above principle can be extended to other combinations for detecting sugar concentration in urine, and quality control of liquids in the future.

10 Conclusion

This work presents POLySight, a novel material sensing solution based on mmWave polarimetric SAR to extract polarization of the signals reflected from objects. We first perform a measurement study at mmWave frequencies to demonstrate how materials express their polarization behavior in the signals reflected after arriving at high incident angles. Our solution extracts this polarization behavior by developing phase-level synchronization framework to augment a large aperture bi-static radar from smaller monostatic COTS FMCW mmWave radars. We develop high resolution SAR imaging that characterizes and classifies materials. We evaluated POLySight across 23 solids, 8 liquids, and 4 powders achieving 95.74%, 96.5% and 100% accuracy in classifying them correctly.

References

[1] accessed Apr. 28, 2025. TerraSAR-X and TanDEM-X. https://earth.esa.int/eogateway/missions/terrasar-x-and-tandem-x.

[2] accessed Apr. 28, 2025. ThruWave- Automated 3D mmWave Scanning. https://www.thruwave.com/.

[3] Mohamed A. Abou-Khousa and Mohammed Saif ur Rahman. 2021. Covered Cracks Detection Using Dual-Polarization Synthetic Aperture Radar Imaging. *IEEE Transactions on Instrumentation and Measurement* 70 (2021), 1–4. https://doi.org/10.1109/TIM.2021.3088468

[4] Mohamed A. Abou-Khousa, Mohammed Saif Ur Rahman, Kristen M. Donnell, and Mohammad Tayeb Al Qaseer. 2023. Detection of Surface Cracks in Metals Using Microwave and Millimeter-Wave Nondestructive Testing Techniques—A Review. *IEEE Transactions on Instrumentation and Measurement* 72 (2023), 1–18. https://doi.org/10.1109/TIM.2023.3238036

[5] Sayed Saad Afzal, Atsutse Kludze, Subhajit Karmakar, Ranveer Chandra, and Yasaman Ghasempour. 2023. AgriTera: Accurate Non-Invasive Fruit Ripeness Sensing via Sub-Terahertz Wireless Signals. In *Proceedings of the 29th Annual International Conference on Mobile Computing and Networking* (Madrid, Spain) *(ACM MobiCom '23)*. Association for Computing Machinery, New York, NY, USA, Article 61, 15 pages. https://doi.org/10.1145/3570361.3613275

[6] Donald K. Atwood and Laetitia Thirion-Lefevre. 2018. Polarimetric Phase and Implications for Urban Classification. *IEEE Transactions on Geoscience and Remote Sensing* 56, 3 (2018), 1278–1289. https://doi.org/10.1109/TGRS.2017.2750211

[7] W.-M. Boerner, H. Mott, and E. Luneburg. 1997. Polarimetry in remote sensing: basic and applied concepts. In *IGARSS'97. 1997 IEEE International Geoscience and Remote Sensing Symposium Proceedings. Remote Sensing - A Scientific Vision for Sustainable Development*, Vol. 3. 1401–1403 vol.3. https://doi.org/10.1109/IGARSS.1997.606459

[8] Ashutosh Dhekne, Mahanth Gowda, Yixuan Zhao, Haitham Hassanieh, and Romit Roy Choudhury. 2018. LiquID: A Wireless Liquid IDentifier. In *Proceedings of the 16th Annual International Conference on Mobile Systems, Applications, and Services* (Munich, Germany) *(MobiSys '18)*. Association for Computing Machinery, New York, NY, USA, 442–454. https://doi.org/10.1145/3210240.3210345

[9] Laura Dodds, Hailan Shanbhag, Junfeng Guan, Saurabh Gupta, and Haitham Hassanieh. 2024. Around the Corner mmWave Imaging in Practical Environments. In *Proceedings of the 30th Annual International Conference on Mobile Computing and Networking* (Washington D.C., DC, USA) *(ACM MobiCom '24)*. Association for Computing Machinery, New York, NY, USA, 953–967. https://doi.org/10.1145/3636534.3690671

[10] Chao Feng, Jie Xiong, Liqiong Chang, Ju Wang, Xiaojiang Chen, Dingyi Fang, and Zhanyong Tang. 2019. WiMi: Target Material Identification with Commodity Wi-Fi Devices. In *2019 IEEE 39th International Conference on Distributed Computing Systems (ICDCS)*. 700–710. https://doi.org/10.1109/ICDCS.2019.00075

[11] E. Fishler, A. Haimovich, R. Blum, D. Chizhik, L. Cimini, and R. Valenzuela. 2004. MIMO radar: an idea whose time has come. In *Proceedings of the 2004 IEEE Radar Conference (IEEE Cat. No.04CH37509)*. 71–78. https://doi.org/10.1109/NRC.2004.1316398

[12] G. Franceschetti and R. Lanari. 2018. *Synthetic Aperture Radar Processing*. CRC Press. https://books.google.com/books?id=7koPEAAAQBAJ

[13] Akshay Gadre, Deepak Vasisht, Nikunj Raghuvanshi, Bodhi Priyantha, Manikanta Kotaru, Swarun Kumar, and Ranveer Chandra. 2022. MiLTOn: Sensing Product Integrity without Opening the Box using Non-Invasive Acoustic Vibrometry. In *2022 21st ACM/IEEE International Conference on Information Processing in Sensor Networks (IPSN)*. 390–402. https://doi.org/10.1109/IPSN54338.2022.00038

[14] Unsoo Ha, Junshan Leng, Alaa Khaddaj, and Fadel Adib. 2020. Food and Liquid Sensing in Practical Environments using RFIDs. In *17th USENIX Symposium on Networked Systems Design and Implementation (NSDI 20)*. USENIX Association, Santa Clara, CA, 1083–1100. https://www.usenix.org/conference/nsdi20/presentation/ha

[15] D.H. Hoekman and M.A.M. Vissers. 2003. A new polarimetric classification approach evaluated for agricultural crops. *IEEE Transactions on Geoscience and Remote Sensing* 41, 12 (2003), 2881–2889. https://doi.org/10.1109/TGRS.2003.817795

[16] AM Horne and G Yates. 2002. Bistatic synthetic aperture radar. In *RADAR 2002*. IET, 6–10.

[17] Yongzhi Huang, Kaixin Chen, Yandao Huang, Lu Wang, and Kaishun Wu. 2021. Vi-liquid: unknown liquid identification with your smartphone vibration. In *Proceedings of the 27th Annual International Conference on Mobile Computing and Networking* (New Orleans, Louisiana) *(MobiCom '21)*. Association for Computing Machinery, New York, NY, USA, 174–187. https://doi.org/10.1145/3447993.3448621

[18] Chengkun Jiang, Junchen Guo, Yuan He, Meng Jin, Shuai Li, and Yunhao Liu. 2020. mmVib: micrometer-level vibration measurement with mmwave radar. In *Proceedings of the 26th Annual International Conference on Mobile Computing and Networking* (London, United Kingdom) *(MobiCom '20)*. Association for Computing Machinery, New York, NY, USA, Article 45, 13 pages. https://doi.org/10.1145/3372224.3419202

[19] Gerhard Krieger, Alberto Moreira, Hauke Fiedler, Irena Hajnsek, Marian Werner, Marwan Younis, and Manfred Zink. 2007. TanDEM-X: A Satellite Formation for High-Resolution SAR Interferometry. *IEEE Transactions on Geoscience and Remote Sensing* 45, 11 (2007), 3317–3341. https://doi.org/10.1109/TGRS.2007.900693

[20] James Lamb. 1996. Miscellaneous data on materials for millimetre and submillimetre optics. *International Journal of Infrared and Millimeter Waves* 17 (12 1996), 1997–2034. https://doi.org/10.1007/BF02069487

[21] Hans J Liebe, George A Hufford, and Takeshi Manabe. 1991. A model for the complex permittivity of water at frequencies below 1 THz. *International Journal of Infrared and Millimeter Waves* 12 (1991), 659–675.

[22] David Long and Fawwaz Ulaby. 2015. *Microwave radar and radiometric remote sensing*. Artech.

[23] Carlos López-Martínez and Xavier Fabregas. 2003. Polarimetric SAR speckle noise model. *IEEE Transactions on Geoscience and Remote Sensing* 41, 10 (2003), 2232–2242.

[24] KE Mattar and HA Buckmaster. 1990. 25 degrees C complex permittivity of water from 65 to 75 GHz. *Journal of Physics D: Applied Physics* 23, 11 (1990), 1464.

[25] H. McNairn and B. Brisco. 2004. The application of C-band polarimetric SAR for agriculture: a review. *Canadian Journal of Remote Sensing* 30, 3 (2004), 525–542. https://doi.org/10.5589/m03-069 arXiv:https://doi.org/10.5589/m03-069

[26] S. M. Hossein Naghavi, Morteza Tavakoli Taba, Mohammed Aseeri, and Ehsan Afshari. 2024. An Integrated 100-GHz FMCW Imaging Radar for Low-Cost Drywall Inspection. *IEEE Transactions on Microwave Theory and Techniques* 72, 2 (2024), 1070–1084. https://doi.org/10.1109/TMTT.2023.3305076

[27] JR Peacock. 2009. Millimetre wave permittivity of water near 25° C. *Journal of Physics D: Applied Physics* 42, 20 (2009), 205501.

[28] K. Sato, H. Kozima, H. Masuzawa, T. Manabe, T. Ihara, Y. Kasashima, and K. Yamaki. 1995. Measurements of reflection characteristics and refractive indices of interior construction materials in millimeter-wave bands. In *1995 IEEE 45th Vehicular Technology Conference. Countdown to the Wireless Twenty-First Century*, Vol. 1. 449–453 vol.1. https://doi.org/10.1109/VETEC.1995.504907

[29] Hailan Shanbhag, Sohrab Madani, Akhil Isanaka, Deepak Nair, Saurabh Gupta, and Haitham Hassanieh. 2023. Contactless material identification with millimeter wave vibrometry. In *Proceedings of the 21st Annual International Conference on Mobile Systems, Applications and Services*. 475–488.

[30] Fei Shang, Panlong Yang, Yubo Yan, and Xiang-Yang Li. 2022. LiqRay: non-invasive and fine-grained liquid recognition system. In *Proceedings of the 28th Annual International Conference on Mobile Computing And Networking* (Sydney, NSW, Australia) *(MobiCom '22)*. Association for Computing Machinery, New York, NY, USA, 296–309. https://doi.org/10.1145/3495243.3560540

[31] Jayanti J. Sharma, Irena Hajnsek, Konstantinos P. Papathanassiou, and Alberto Moreira. 2011. Polarimetric Decomposition Over Glacier Ice Using Long-Wavelength Airborne PolSAR. *IEEE Transactions on Geoscience and Remote Sensing* 49, 1 (2011), 519–535. https://doi.org/10.1109/TGRS.2010.2056692

[32] Bangjie Sun, Sean Rui Xiang Tan, Zhiwei Ren, Mun Choon Chan, and Jun Han. 2022. Detecting counterfeit liquid food products in a sealed bottle using a smartphone camera. In *Proceedings of the 20th Annual International Conference on Mobile Systems, Applications and Services* (Portland, Oregon) *(MobiSys '22)*. Association for Computing Machinery, New York, NY, USA, 42–55. https://doi.org/10.1145/3498361.3539776

[33] Ju Wang, Jie Xiong, Xiaojiang Chen, Hongbo Jiang, Rajesh Krishna Balan, and Dingyi Fang. 2017. TagScan: Simultaneous Target Imaging and Material Identification with Commodity RFID Devices. In *Proceedings of the 23rd Annual International Conference on Mobile Computing and Networking* (Snowbird, Utah, USA) *(MobiCom '17)*. Association for Computing Machinery, New York, NY, USA, 288–300. https://doi.org/10.1145/3117811.3117830

[34] Zhu Wang, Yifan Guo, Zhihui Ren, Wenchao Song, Zhuo Sun, Chao Chen, Bin Guo, and Zhiwen Yu. 2024. LiqDetector: Enabling Container-Independent Liquid Detection with mmWave Signals Based on a Dual-Reflection Model. *Proc. ACM Interact. Mob. Wearable Ubiquitous Technol.* 7, 4, Article 186 (Jan. 2024), 24 pages.

https://doi.org/10.1145/3631443

[35] Chenshu Wu, Feng Zhang, Beibei Wang, and K. J. Ray Liu. 2020. mSense: Towards Mobile Material Sensing with a Single Millimeter-Wave Radio. *Proc. ACM Interact. Mob. Wearable Ubiquitous Technol.* 4, 3, Article 106 (Sept. 2020), 20 pages. https://doi.org/10.1145/3411822

[36] Binbin Xie, Jie Xiong, Xiaojiang Chen, Eugene Chai, Liyao Li, Zhanyong Tang, and Dingyi Fang. 2019. Tagtag: material sensing with commodity RFID. In *Proceedings of the 17th Conference on Embedded Networked Sensor Systems* (New York, New York) *(SenSys '19)*. Association for Computing Machinery, New York, NY, USA, 338–350. https://doi.org/10.1145/3356250.3360027

[37] Dawei Yan, Panlong Yang, Fei Shang, Weiwei Jiang, and Xiang-Yang Li. 2024. Wi-Painter: Fine-grained Material Identification and Image Delineation Using COTS WiFi Devices. *Proc. ACM Interact. Mob. Wearable Ubiquitous Technol.* 7, 4, Article 203 (Jan. 2024), 25 pages. https://doi.org/10.1145/3633809

[38] Muhammet Emin Yanik and Murat Torlak. 2019. Near-Field 2-D SAR Imaging by Millimeter-Wave Radar for Concealed Item Detection. In *2019 IEEE Radio and Wireless Symposium (RWS)*. 1–4. https://doi.org/10.1109/RWS.2019.8714552

[39] Muhammet Emin Yanik, Dan Wang, and Murat Torlak. 2020. Development and Demonstration of MIMO-SAR mmWave Imaging Testbeds. *IEEE Access* 8 (2020), 126019–126038. https://doi.org/10.1109/ACCESS.2020.3007877

[40] Hui-Shyong Yeo, Gergely Flamich, Patrick Schrempf, David Harris-Birtill, and Aaron Quigley. 2016. RadarCat: Radar Categorization for Input & Interaction. In *Proceedings of the 29th Annual Symposium on User Interface Software and Technology* (Tokyo, Japan) *(UIST '16)*. Association for Computing Machinery, New York, NY, USA, 833–841. https://doi.org/10.1145/2984511.2984515

[41] Shichao Yue and Dina Katabi. 2019. Liquid Testing with Your Smartphone. In *Proceedings of the 17th Annual International Conference on Mobile Systems, Applications, and Services* (Seoul, Republic of Korea) *(MobiSys '19)*. Association for Computing Machinery, New York, NY, USA, 275–286. https://doi.org/10.1145/3307334.3326078

[42] Jonghyuk Yun, Kyoosik Lee, Kichang Lee, Bangjie Sun, Jaeho Jeon, Jeonggil Ko, Inseok Hwang, and Jun Han. 2024. PowDew: Detecting Counterfeit Powdered Food Products using a Commodity Smartphone. In *Proceedings of the 22nd Annual International Conference on Mobile Systems, Applications and Services* (Minato-ku, Tokyo, Japan) *(MOBISYS '24)*. Association for Computing Machinery, New York, NY, USA, 210–222. https://doi.org/10.1145/3643832.3661877

[43] Diana Zhang, Jingxian Wang, Junsu Jang, Junbo Zhang, and Swarun Kumar. 2019. On the feasibility of wi-fi based material sensing. In *The 25th Annual International Conference on Mobile Computing and Networking*. 1–16.

[44] Kai Zheng, Wuqiong Zhao, Timothy Woodford, Renjie Zhao, Xinyu Zhang, and Yingbo Hua. 2024. Enhancing mmWave Radar Sensing Using a Phased-MIMO Architecture. In *Proceedings of the 22nd Annual International Conference on Mobile Systems, Applications and Services* (Minato-ku, Tokyo, Japan) *(MOBISYS '24)*. Association for Computing Machinery, New York, NY, USA, 56–69. https://doi.org/10.1145/3643832.3661865

[45] Tianyue Zheng, Zhe Chen, Jun Luo, Lin Ke, Chaoyang Zhao, and Yaowen Yang. 2021. SiWa: see into walls via deep UWB radar. In *Proceedings of the 27th Annual International Conference on Mobile Computing and Networking* (New Orleans, Louisiana) *(MobiCom '21)*. Association for Computing Machinery, New York, NY, USA, 323–336. https://doi.org/10.1145/3447993.3483258